ADVANCED FUNCTIONAL MATERIALS
www.afm-journal.de

Integrated High-Entropy Alloy Nanowire/Carbon Nanotube Membrane Electrode for Efficient Hydrogen Evolution in Acid Solution

Hao Yang, Zichu Zhang, Zhaoming Wang, Feng Zhang, Shaokang Liu, Lili Zhang, Chao Shi, Peng-Xiang Hou, Hui-Ming Cheng, Xiao Wang,* and Chang Liu**

Proton exchange membrane water electrolysis is one of the most promising techniques for industrial green hydrogen production. However, the electrocatalysts for hydrogen production have suffered from low activity and poor durability in acidic environment. Here an integrated membrane electrode composed of N-doped carbon-coated high-entropy nanowires (HEA NWs) anchored on a single-walled carbon nanotube (SWCNT) network is reported for efficient and stable hydrogen evolution reaction (HER). The residue surfactant remaining on the HEA NWs prepared by a wet chemistry method is transformed to a N-doped carbon layer when fast heating the HEA NWs loaded on a SWCNT film, which firmly connects the ultrathin HEA NWs with SWCNT bundles. When used as an integrated membrane electrode, the hybrid film showed not only a low overpotential of 42 mV at 100 mA cm^{-2} for HER but also excellent durability up to 1000 h at 500 mA cm^{-2} in acid solution. The desirable performance is attributed to the hierarchical structure of the membrane electrode, where 1D HEA NWs anchored on SWCNT network function in regulating the hydrogen adsorption of H^*, facilitating electron transfer, and protecting the nanowires from degradation.

1. Introduction

The ever-increasing energy consumption and severe environmental pollution issues require clean energy to replace the traditional fossil energy.[1] Hydrogen is an ideal green energy carrier for low-carbon society because it has both high energy density and environmental friendliness.[2] To achieve the low-cost mass production of green H_2, proton exchange membrane water electrolysis (PEMWE) has been considered one of the most promising techniques, owing to its high conversion efficiency (80–90%) and high H_2 purity (>99.99%).[3] However, the problems of metal-based electrocatalyst dissolution, active composition detachment, catalyst nanoparticle aggregation, and corrosion of the metal foam supports, have hampered the practical application of PEMWE.[4] Therefore, developing low-cost electrocatalysts with high activity and long-term durability are highly desired to facilitate the green H_2 production.

Tremendous efforts have been devoted to designing and preparing novel electrocatalysts for PEMWE. As state-of-the-art electrocatalysts, ultrafine noble metals, bimetallic alloys, and high-entropy alloys (HEA) have been investigated as potential candidates.[5] It was reported that HEA nanoparticles (NPs) showed very high hydrogen evolution reaction (HER) catalysis activity, which was ascribed to their abundant active sites, tunable electronic structures, and synergistic effects of HEA metal elements.[6] However, these metal NPs supported on conductive supports usually suffer from dissolution, detachment, and aggregation, leading to poor durability in an acidic environment.[7] Therefore, protective layers are necessary to prevent the degradation of the ultrafine electrocatalysts. It was reported that silica and carbon coating layers were effective in preventing the dissolution and aggregation.[8] However, organic binders are needed to stick these powder catalysts onto a conductive support, and H_2 bubbles yielded would detach the NPs during long-term operation.[9] Additionally, the commonly used metal foam supports are not applicable in PEMWE under acidic conditions.[10]

Compared to the commonly used metal supports, single-walled carbon nanotube (SWCNT) have higher strength, larger surface area, and excellent chemical stability in acid solution.[11]

H. Yang, Z. Zhang, F. Zhang, S. Liu, L. Zhang, C. Shi, P.-X. Hou, H.-M. Cheng, C. Liu
Shenyang National Laboratory for Materials Science
Institute of Metal Research
Chinese Academy of Sciences
72 Wenhua Road, Shenyang 110016, China
E-mail: fengzhang@imr.ac.cn; cliu@imr.ac.cn

H. Yang
School of Materials Science and Engineering
Shenyang University of Technology
Shenyang 110870, China

Z. Zhang, F. Zhang, S. Liu, L. Zhang, P.-X. Hou, C. Liu
School of Materials Science and Engineering
University of Science and Technology of China
Hefei 230026, China

Z. Wang, H.-M. Cheng, X. Wang
Institute of Technology for Carbon Neutrality
Shenzhen Institutes of Advanced Technology
Chinese Academy of Sciences
Shenzhen 518055, China
E-mail: xiao.wang@siat.ac.cn

The ORCID identification number(s) for the author(s) of this article can be found under https://doi.org/10.1002/adfm.202425156

DOI: 10.1002/adfm.202425156

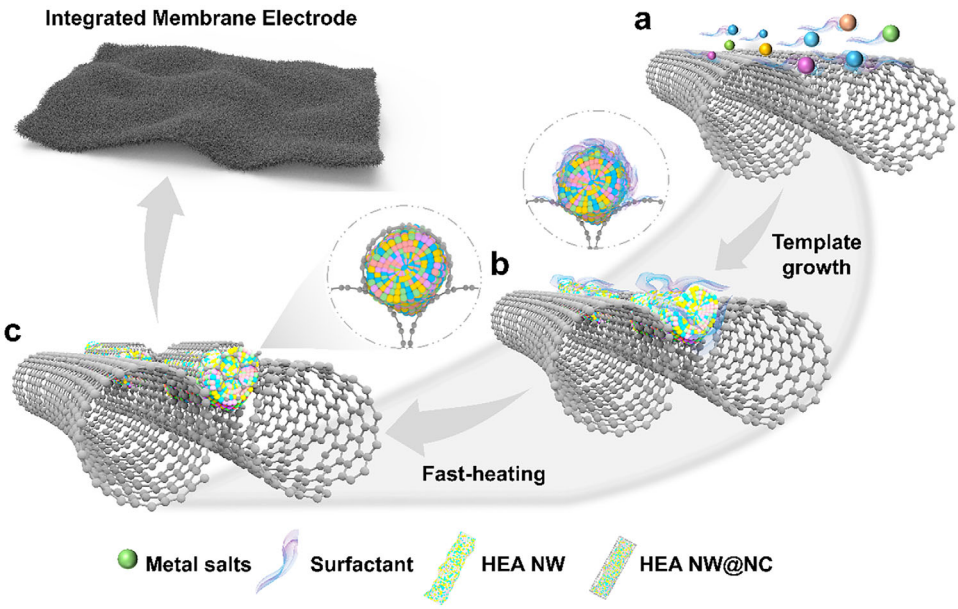

Figure 1. Schematic showing the fabrication process of HEA NW@NC/SWCNT hybrid films.

In addition, SWCNT bundles are also an ideal template guiding the growth of nanocrystals with specific orientations and electronic structures.[12] Therefore, macroscopic SWCNT films composed of entangled bundles can be an ideal electrocatalyst support. For instance, Liu et al. reported a flexible self-standing membrane electrode composed of Ni NPs anchored on SWCNT networks that showed a high HER electrocatalytic activity in alkaline media with a overpotential of 190 mV at 10 mA cm^{-2}.[13] Recently, they prepared a hybrid film electrode comprising HEA nanowires (NWs) and SWCNTs, and only 26 mV was required to reach a current density of 10 mA cm^{-2} for HER in alkaline conditions.[14] Although progresses have been made, achieving high activity and long-term durability simultaneously in acidic condition remains a big challenge due to the weak interaction between the SWCNT support and loaded electrocatalysts.

Here we report an integrated membrane electrode composed of N-doped carbon-coated ultrathin HEA NWs anchored on SWCNT network. Monodispersed 1D HEA NWs were loaded on SWCNT bundles by a wet chemical method, during which residue surfactant was coated on the surface of the HEA NWs. N-doped carbon layer was then formed by the decomposition of the surfactant through fast heating (22.5 °C s^{-1}) treatment of the HEA NWs-loaded SWCNTs. The obtained freestanding hybrid film was directly used as an integrated membrane electrode, which exhibited excellent HER durability of 1000 h at a current density of 500 mA cm^{-2}, and an extremely low overpotential of 42 mV was required to reach 100 mA cm^{-2} (112 mV for Pt/C) in 0.5 M H_2SO_4 solution. Density functional theory (DFT) calculations indicated that the strain originating from the interaction between the N-doped carbon shell and HEA NWs modulates the binding energy of H^* intermediates. Furthermore, the HEA NWs are firmly anchored on SWCNT bundles through the N-doped carbon layers and therefore, the integrated membrane electrode promotes electron transfer and protects the HEA from degradation in harsh acidic conditions.

2. Results and Discussion

2.1. Synthesis and Structural Characterizations

Figure 1 illustrates the fabrication process of the integrated membrane electrode composed of N-doped carbon-coated ultrathin HEA NWs and SWCNT bundles. By using a wet-chemistry synthesis method, metal acetylacetonates mixed with surfactant were dissolved in oleylamine for growing HEA NWs,[14] while SWCNT networks were used as a template to load the HEA NWs (Figure 1a). As shown in Figure S1 (Supporting Information), monodispersed ultrathin HEA NWs are anchored on the surface of SWCNT bundles, and the orientations of HEA NWs are basically parallel to the axial direction of SWCNT bundles. The obtained HEA NW/SWCNT hybrid was wrapped with a layer of surfactants and residual oleyl amine (Figure 1b). Fast heating was performed to carbonize the residue surfactant and organic solvents in a short time. As a result, N-doped carbon shells were formed at the interface between HEA NWs and SWCNTs without involving additional carbon and nitrogen precursors (Figure 1c). The HEA NWs were anchored on the SWCNTs by the N-doped carbon shells, and a free-standing integrated HEA NW@NC/SWCNT hybrid film was obtained. Owing to the fast ramp-up rate and ultrashort heating time, the HEA NWs will retain their original 1D structure. This method not only efficiently eliminates the residual organics that may block the active catalysis sites on HEA NWs but also leads to the formation of N-doped carbon shells that will connect the HEA NWs and SWCNT bundles.

Photographs of a free-standing HEA NW@NC/SWCNT film and a HEA NW@NC/SWCNT foam are shown in **Figures 2a** and S2 (Supporting Information), respectively. To evaluate their hydrophilicity, we measured the contact angle of water on the surface of the HEA NW@NC/SWCNT and HEA NW/SWCNT hybrids. The HEA NW@NC/SWCNT macrostructure exhibited

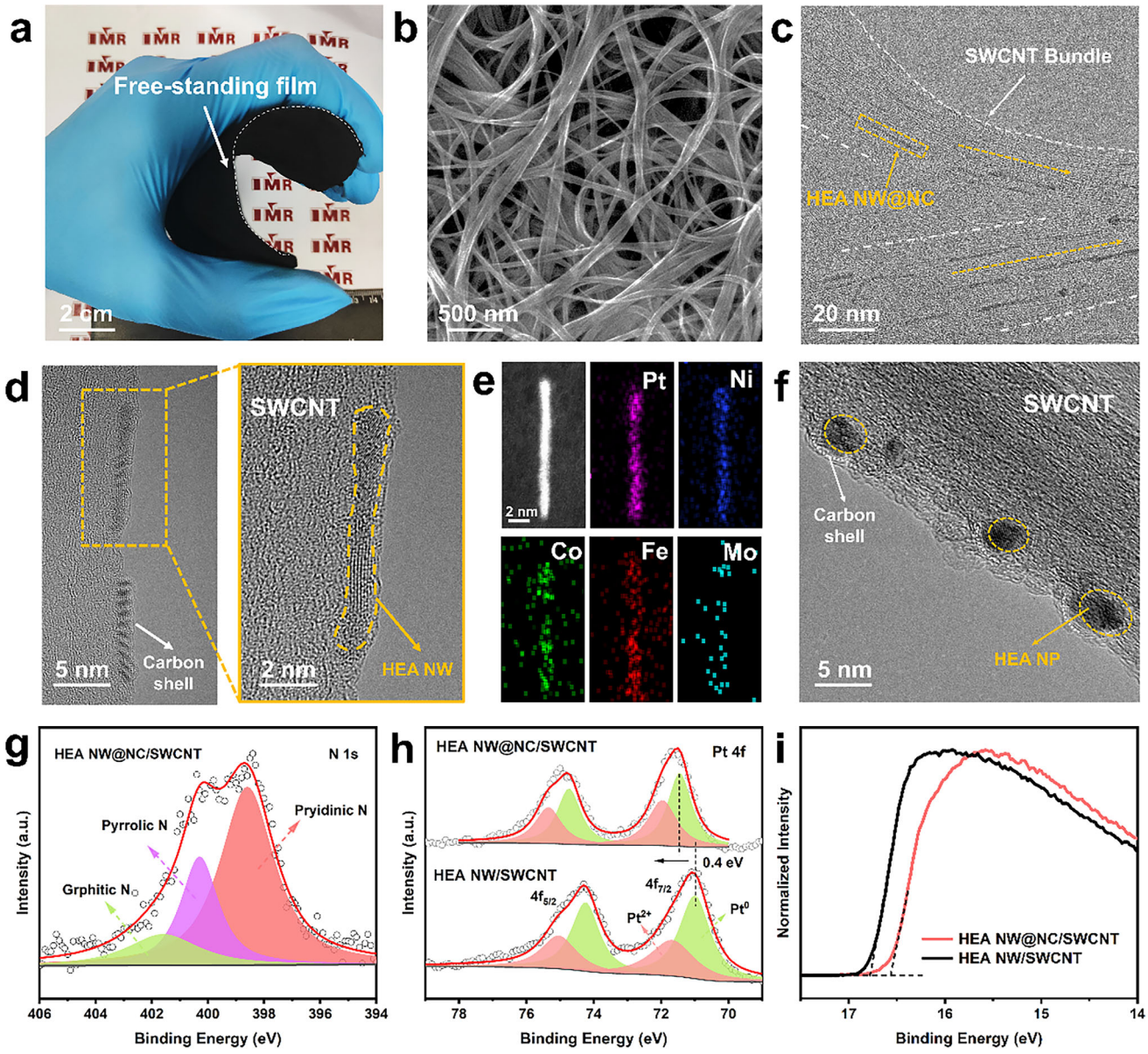

Figure 2. a) Optical image of the HEA NW@NC/SWCNT film. b) SEM image, c,d) TEM images, and e) EDS mapping of HEA NWs@NC/SWCNT. f) TEM image of the HEA NP@NC/SWCNT. g) N 1s XPS spectra of HEA NW@NC/SWCNT. h) Pt 4f XPS spectra and i) UPS spectra of HEA NW@NC/SWCNT and HEA NW/SWCNT.

excellent hydrophilicity with a water contact angle of 27.2°. On the other hand, the contact angle of HEA NW/SWCNT was 80.2° (Figure S3, Supporting Information), indicating that the formation of N-doped carbon layer through fast-heating treatment is important to improve the hydrophilicity. N_2 adsorption/desorption was performed to characterize the specific surface area and pore structures of HEA NW@NC/SWCNT film. As shown in Figure S4 (Supporting Information), a typical IV isotherm with a large hysteresis loop at $P/P_0 > 0.5$ was observed, demonstrating the existence of abundant mesopores. Compared with HEA NW/SWCNT, there are also more micropores (< 2 nm) detected in the HEA NW@NC/SWCNT, which may be formed during the fast pyrolysis of residue surfactant and organic solvents.

Figure 2b shows scanning electron microscope (SEM) image of the HEA NW@NC/SWCNT film, we can see that the SWCNT bundles are clean, and very few organic residues can be observed, which is also confirmed by Fourier transform infrared spectroscopy (FT-IR) analysis (Figure S5, Supporting Information). Transmission electron microscope (TEM) observation (Figure 2c) shows that most monodispersed ultrathin NWs are parallelly anchored on the SWCNT bundles. The average diameter of the HEA NWs is 1.7 nm (Figure S6, Supporting Information), confirming that the HEA NWs have ultrathin diameters and high specific

surface area. High-resolution TEM (HRTEM) image (Figure 2d) reveals that the HEA NWs are covered with a carbon shell thinner than 1.0 nm. X-ray energy-dispersive spectroscopy (EDS) elemental mappings and spectrum (Figure 2e; Figure S7, Supporting Information) were measured to analyze the chemical composition of the HEA NWs, we can see that Pt, Fe, Co, Ni, and Mo are homogeneously distributed in the HEA NWs of HEA NW@NC/SWCNT. Additionally, inductively coupled plasma optical emission spectroscopy (ICP-OES) further confirms the polymetallic composition of the HEA NWs (Figure S8, Supporting Information), and the atomic ratio of Pt: Fe: Co: Ni: Mo is calculated to be 27:34:9:8:22.

As shown in Figure 2c and Figures S9 and S10 (Supporting Information), most HEA NWs have a consistent orientation along the axis of SWCNT bundles, this is because that SWCNT bundles are a guidance template for the controlled growth of HEA NWs in wet chemical synthesis. To investigate the function of SWCNT in the oriented growth, graphene was used as a contrasting support for the synthesis of HEA NWs for comparison. We can see that the orientation of HEA NWs obtained is disordered (Figure S11, Supporting Information). Therefore, the SWCNT bundles play a crucial role in determining the growth orientation of 1D HEA NWs. Other than template, fast heating is another essential factor for the synthesis of integrated HEA NW@NC/SWCNT films, HEA NWs maintain their nanowire structure after being heated with a high heating rate of 22.5 °C s^{-1}. In contrast, only HEA NPs coated with shells (HEA NP@NC/SWCNT) were obtained when the heating rate was decreased to 10.0 °C min^{-1} (Figure 2f). Slow heating rate results in long heating time, and the aggregation HEA NWs occurred. However, under fast heating and short-duration conditions, the surface atoms do not have sufficient time to agglomerate, allowing the HEA NWs to retain their original 1D structures.[15] Hence, the SWCNT bundle template and fast-heating technique are critical for the preparation of integrated HEA NW@NC/SWCNT hybrid films.

To characterize the phase of HEA NWs after fast heating, X-ray diffraction (XRD) measurement was performed. The characteristic peaks in the XRD patterns (Figure S12, Supporting Information) are ascribed to the face-centered cubic (*fcc*) structure of Pt (PDF#04-0802), and the positive shifts of peaks in the XRD patterns imply the formation of HEA.[16] Besides, the characteristic peaks of HEA NW@NC/SWCNT were observed to shift to higher angles than for HEA NW/SWCNT, indicating the presence of partial lattice compression in the HEA NWs, which is ascribed to the moderating effect of the N-doped carbon shell.[17] We analyzed the surface chemical composition of HEA NW@NC/SWCNT film by using X-ray photoelectron spectroscopy (XPS). As shown in Figure S13 (Supporting Information), HEA metals, C, O, and N are detected, and the content of N is calculated to be 5.1 at.%. As shown in the high-resolution N 1s spectrum (Figure 2g), pyridine N (398.6 eV), pyrrolic N (400.2 eV), and graphitic-N (401.7 eV) are detected. Among these N species, pyridinic-N and pyrrolic-N are dominant due to the short heating time of 30 s and relatively low carbonization temperature of 700 °C. High-resolution C 1s spectrum also shows the presence of the C—N bond (Figure S13b, Supporting Information), suggesting that the N-doped carbon shell was formed by the decomposition of residual surfactant during the fast-heating. To analyze the chemical state of Pt, Pt 4f peaks are deconvoluted into two doublets assigned to Pt^0 and Pt^{2+} (Figure 2h), the binding energy of the Pt^0 peak in HEA NW@NC/SWCNT exhibits a blue shift of ≈0.4 eV, in comparison to that of HEA NW/SWCNT. This suggests electron transfer from Pt to carbon shell and the shift of the d-band center, achieved by the connection between carbon shells and the HEA NW.[18] Additionally, we measured the work functions of the HEA NW@NC/SWCNT and HEA NW/SWCNT using ultraviolet photoelectron spectroscopy (UPS). As shown in Figure 2i, the cutoff edge of HEA NW@NC/SWCNT (16.56 eV) is more negative than that of HEA NW/SWCNT (16.78 eV). Hence, HEA NW@NC/SWCNT has a higher work function and a lower Fermi level, facilitating electron transfer from HEA NWs to the N-doped carbon shells.[19]

2.2. HER Performance Evaluation in Acid Solution

The free-standing, hydrophilic, porous HEA NW@NC/SWCNT film was used as an integrated membrane electrode for HER in acid solution. To evaluate the HER activity of HEA NW@NC/SWCNT film, HEA NP@NC/SWCNT, HEA NW/SWCNT, and commercial 20% Pt/C were also tested for comparison. Their HER activities were evaluated by linear sweep voltammetry (LSV) at a scanning rate of 5 mV s^{-1} in 0.5 M H_2SO_4 at room temperature (25 °C). As shown in **Figures 3a** and S14 (Supporting Information), an overpotential of 42 mV is required for HEA NW@NC/SWCNT to achieve a current density of 100 mA cm^{-2}, which is much lower than those of the reference catalysts (72 mV for HEA NW/SWCNT, 83 mV for Pt NW@NC/SWCNT, 96 mV for HEA NP@NC/SWCNT, and 112 mV for Pt/C). The high HER activity (lowest overpotential) of HEA NW@NC/SWCNT is ascribed to the N-doped carbon shell, unique nanowire structure, and high-entropy effects of HEA NWs (Figure S15, Supporting Information). Furthermore, the fast-heating and washing processes eliminate organic residues, thereby exposing more activity sites and improving the conductivity, as evidenced by the superior HER activity of HEA NW@NC/SWCNT (Figure S16, Supporting Information). The Tafel slope of HEA NW@NC/SWCNT, HEA NW/SWCNT, HEA NP@NC/SWCNT, and Pt/C are calculated to be 21.2, 30.6, 44.1, and 37.1 mV dec^{-1}, respectively (Figure 3b). The low Tafel slope of HEA NW@NC/SWCNT indicates a fast HER kinetics through the Volmer-Tafel reaction route.[9a] Electrochemical impedance spectra (EIS) were measured to analyze the Nyquist plots (Figure 3c). The smallest semicircle diameter in the Nyquist plot of the HEA NW@NC/SWCNT demonstrates the lowest charge transfer resistance (R_{ct}) of 5.3 Ω (Figure S17, Supporting Information). Moreover, HEA NW@NC/SWCNT exhibits significantly lower Warburg impedance compared to Pt NW@NC/SWCNT, indicating the high-entropy effect of the HEA NW@NC/SWCNT can mitigate the impact of the diffusion process on HER (Figure S18, Supporting Information). This confirms that our integrated membrane electrode composed of N-doped carbon shell connected HEA NWs and SWCNT network promotes electron transfer and enhances the HER kinetics.

Besides fast HER kinetics, our HEA NW@NC/SWCNT also exhibited outstanding intrinsic activity. To calculate the electrochemical active surface area (ECSA), double-layer capacitance

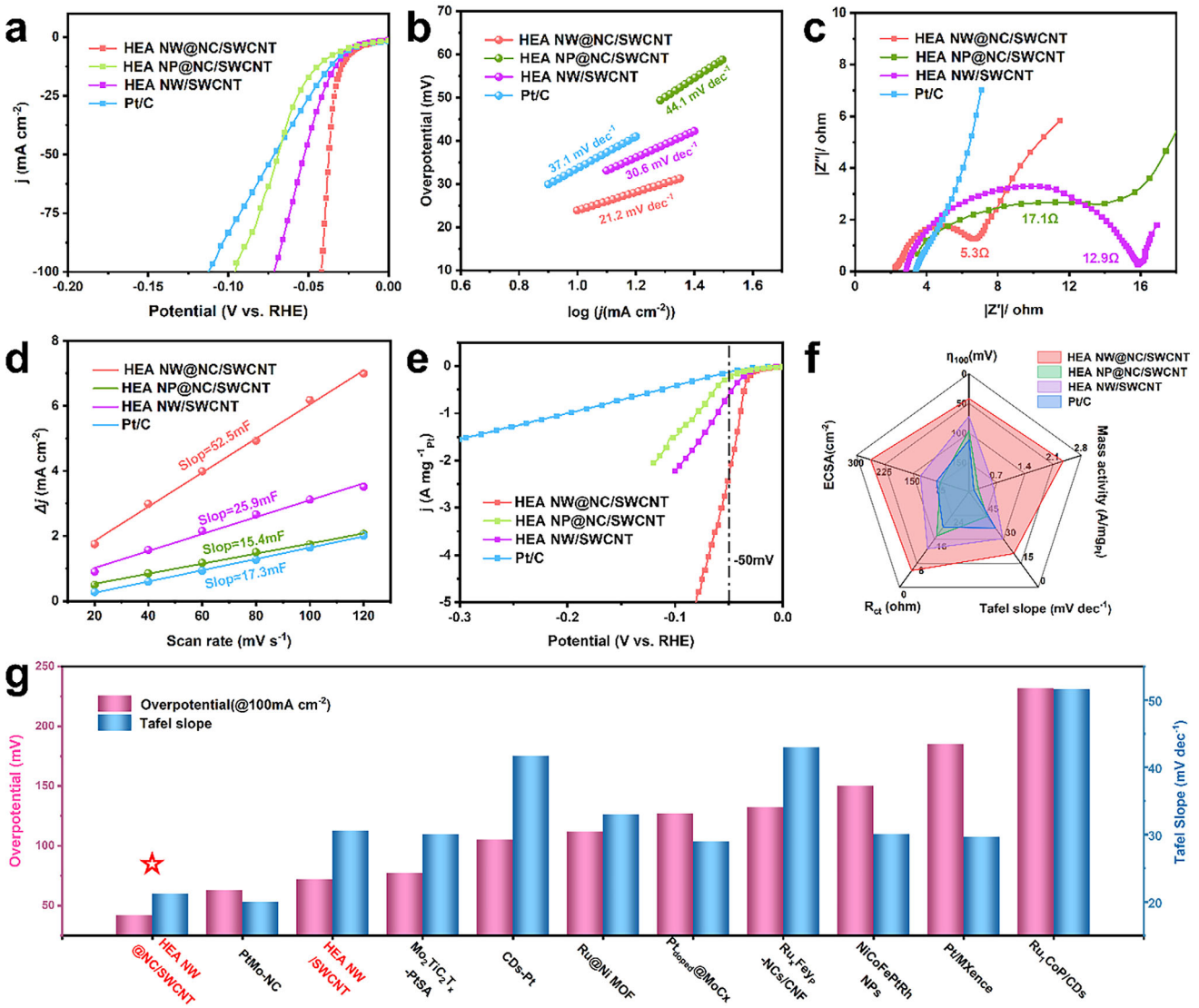

Figure 3. Electrocatalytic HER performance of HEA NW@NC/SWCNT in 0.5 M H_2SO_4. a) LSV curves, b) Tafel slopes, c) EIS spectra, and d) calculated C_{dl} of the HEA NW@NC/SWCNT. e) LSV curves at −50 mV versus RHE normalized by Pt mass loading. f) HER performance of HEA NW@NC/SWCNT, HEA NW@NC/SWCNT, HEA NP@NC/SWCNT, HEA NW/SWCNT and Pt/C. g) HER activities of HEA NW@NC/SWCNT, in comparison with representative reported electrocatalysts in literature.

(C_{dl}) was measured through cyclic voltammograms (CV) testing (Figure S19, Supporting Information). The C_{dl} of HEA NW@NC/SWCNT was calculated to be 52.5 mF cm^{-2}, while the values for HEA NW/SWCNT and HEA NP@NC/SWCNT are 25.9 and 15.4 mF cm^{-2}, respectively (Figure 3d). The ECSA normalized polarization curves show that the HEA NW@NC/SWCNT has a specific activity of 2.36 mA cm^{-2} at an overpotential of 50 mV, which is higher than the other reference catalysts, suggesting that the HEA NW@NC/SWCNT has a high intrinsic HER activity (Figure S20, Supporting Information). This means that more active sites for hydrogen evolution at a given potential are provided for the HEA NW@NC/SWCNT. In addition, the loading of HEA NWs in the HEA NW@NC/SWCNT is 3.53 wt.%, as determined by ICP measurement (Table S1, Supporting Information). The mass activity of the catalyst was calculated by normalizing the current density to the Pt loading weight (Figure 3e). The HEA NW@NC/SWCNT has a mass activity of 2.35 A mg^{-1}_{Pt} at an overpotential of 50 mV, 18 times higher than that of Pt/C (0.12 A mg^{-1}_{Pt}). These results indicate that the HEA NW@NC/SWCNT integrated membrane electrode has higher HER activity than the other reference catalysts (Figure 3f), which can be ascribed to the unique structure of 1D HEA NWs and N-doped carbon shell that enhance the activity of HEA NW@NC/SWCNT. Notably, the low overpotential of HEA NW@NC/SWCNT at 100 mA cm^{-2} in acidic electrolytes and low Tafel slopes impressively surpasses those of the state-of-the-art electrocatalysts reported in literatures (Figure 3g; Table S2, Supporting Information).

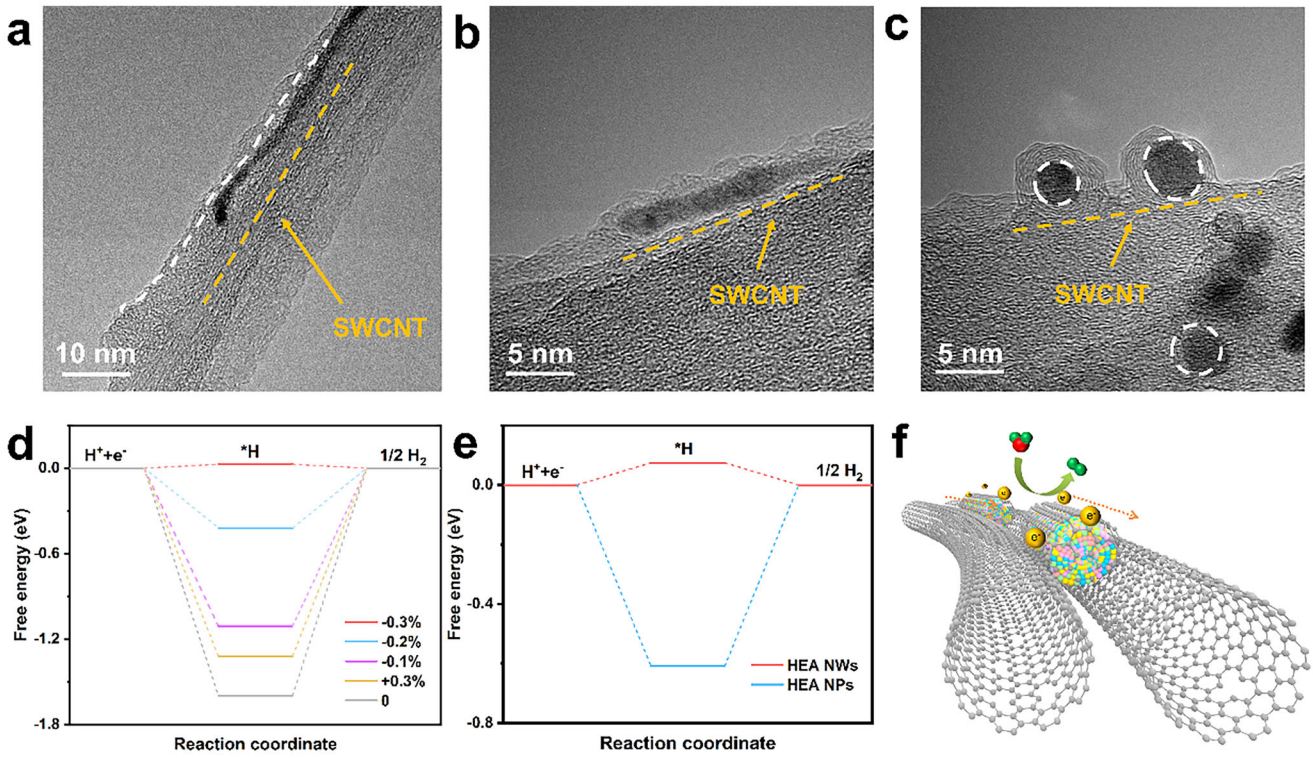

Figure 4. TEM images of HEA NW@NC/SWCNT prepared at different fast-heating temperatures of a) 600, b) 800, and c) 900 °C. d) Calculated ΔG_{H^*} diagram of HER for the HEA NW@NC/SWCNT with different lattice strains. e) Calculated ΔG_{H^*} diagram of HER for HEA NWs and HEA NPs. f) Schematic showing the HER activity enhancement achieved by the HEA NW@NC/SWCNT with a hierarchical structure.

2.3. Origin of the High HER Activity of HEA NW@NC/SWCNT Membrane Electrode

To understand the impact of the structure of HEA NW@NC on its HER activity, HEA NWs coated with N-doped carbon shells with different thicknesses were prepared, and the hybrid films were used as membrane electrode for HER in an acidic solution. The thickness and crystallinity of carbon shells were controlled by changing the temperature and heating rate of the fast-heating process. Carbon shells were observed to form on the surface of HEA NWs and SWCNTs after heat treatment at 600 °C (**Figure 4**a). It was found that the crystallinity of the carbon shell improved significantly when the fast-heating temperature was increased in the range of 600–900 °C. Only metallic NPs coated with thick carbon layer were obtained at 900 °C (Figure 4b,c), suggesting the tendency of NWs aggregation at elevated temperatures. As shown in Figure S21 (Supporting Information), a thin and porous N-doped carbon shell was obtained at 700 °C. Complete pyrolysis of organic residuals occurred at 700 °C leads to a sufficient exposure of active sites and improved HER performance. When fast heated at 800 °C, the carbon shell became dense, leading to a poor contact between active sites and electrolyte and thus, decreased HER activity. When the temperature was further increased to 900 °C, the NWs agglomerated to form large-size NPs coated with dense carbon layers, which exhibited a poor HER activity.[20] As shown in Figure S22 (Supporting Information), the characteristic peaks of HEA NW@NC/SWCNT shift to higher angles with increasing temperature, indicating lattice compression due to compressive strain. This aligns with TEM observations, where enhanced carbon shell crystallinity at elevated temperatures applies external stress, amplifying strain in the HEA NWs. Combined with TEM analysis, the phenomenon can be attributed to an increase in the crystallinity of the carbon shell on the HEA NWs' surface, which enhances external stress and ultimately leads to increased compressive strain in the HEA NWs. At 800 °C, sharper peaks and a distinct peak at 44.5° confirm the formation of PtFe, PtCo, and PtNi alloys.[21] Reduced lattice distortion at this stage diminishes the high-entropy effect, correlating with decreased HER activity.

To understand the origin of the performance improvement achieved by the N-doped carbon shell, HRTEM images were analyzed in detail to identify lattice strain in the HEA NW@NC/SWCNT. Figure S23 (Supporting Information) shows that the average plane spacing of HEA NW@NC across five atom layers is 2.10 Å, while the corresponding value for HEA NWs is 2.11 Å. This demonstrates a compressibility of HEA NWs realized by the coated carbon shells, which agrees well with the XRD patterns.

Based on the above results, we consider that the improved catalytic performance might result from the compressive strain.[22] A slab model was constructed to investigate the relationship between the Gibb free energy of H absorption and the lattice strain. We calculated the ΔG_{H^*} with different lattice strains (−0.3%, −0.2%, −0.1%, 0, +0.3%), where "−" represents compressive strain, while "+" represents tensile strain (Figure S24, Supporting Information). As shown in Figure 4d, the strain

modulates the hydrogen adsorption energy of the HEA NW@NC. The ΔG_{H^*} on HEA NWs without strain involved was calculated to be −1.60 eV. When a compress strain was introduced, the ΔG_{H^*} decreased. As the compressive strain reached 0.3%, ΔG_{H^*} was calculated to be 0.03 eV. Strain caused by the carbon layer leads to local lattice distortion, resulting in dislocation, edge vacancies as well as undercoordinated atoms. These structural modifications at the distorted edge regions could effectively expose additional electrochemically active sites for catalytic reactions. Moreover, compressive strain shifts the d—band center away from the Fermi level, which reduces the energy of antibonding states (σ^*). The low energy of σ^* would weaken the interaction between the reaction intermediate and active sites, facilitating hydrogen adsorption thereby improving the intrinsic activity of active sites (Figure S25, Supporting Information). Hence, the compressive strain leads to suitable adsorption energy between H^* and the active sites, enabling high catalytic activity of the HEA NWs coated with N-doped carbon shells.

As shown in Figure 3a, the HEA NWs show higher activity than HEA NPs. According to experimental results, we optimized the computation model, and the element-top sites were selected for the proton adsorption (Figure S26, Supporting Information). Compared with HEA NPs, HEA NWs have a thermoneutral energy of 0.07 eV for H^* desorption (Figure 4e). Thanks to the 1D structure of HEA NWs, as shown in Figure 4f, suitable hydrogen adsorption and desorption between H^* and HEA NW@NC are demonstrated, achieving fast kinetics and high HER activity.

2.4. Stability of Integrated Membrane Electrodes

CV cycles and chronoamperometry were performed to evaluate the stability of the integrated HEA NW@NC/SWCNT membrane electrode in 0.5 M H_2SO_4 at room temperature (25 °C). **Figure 5a** shows that no discernible decrease in activity loss can be observed for the HEA NW@NC/SWCNT after 10k CV cycles, while HEA NW/SWCNT and Pt/C show apparent negative shifts after 10k cycles. This illustrates that N-doped carbon shell coating endows the HEA NW@NC/SWCNT with superior stability. To assess the long-term durability of HEA NW@NC/SWCNT integrated membrane electrodes, we performed a chronoamperometry test at 500 mA cm^{-2}. As shown in Figure 5b, the decay in current density for the HEA NW@NC/SWCNT is negligible after 1000 h at 500 mA cm^{-2}. In contrast, the current density of HEA NW/SWCNT shows a substantial decrease after 50 h under identical conditions. After a long-term test for 100 h, the contents of Pt, Co, and Fe elements in the electrolyte were below the detection limit of the ICP-MS, and the concentrations of other metallic elements were also extremely low (Table S3, Supporting Information). This result indicates that there was barely any dissolution of HEA NWs, which can be attributed to the covering carbon shells. In addition, this result also confirms that the dissolution and redeposition of Pt from the counter electrode does not influence the working electrode during the electrochemical measurements. These results prove that the ultrathin N-doped carbon shell functions as a protective barrier, effectively mitigating chemical corrosion and mechanical degradation in the HER in acid solution.

To reveal the origin of the excellent stability of the HEA NW@NC/SWCNT membrane electrode, the structural change of the HEA NWs was monitored by TEM along the stability assessment. As shown in Figure 5c, large NPs and a decrease in NWs density were observed, suggesting dissolution and aggregation of exposed HEA NWs after 50 h HER at 500 mA cm^{-2} under acidic conditions (Figure S27, Supporting Information). By contrast, the 1D structure of HEA NW@NC is well-retained, and no degradation of the ultrathin N-doped carbon shell was observed even after 1000 h (Figure 5d; Figure S28, Supporting Information). Thanks to the formation of C—C bonding after carbonization, the N-doped carbon shells well connect the NWs and the SWCNT bundles. The carbon shell serves as an armor, which effectively prevents the aggregation of HEA NWs and inhibits their dissolution, thereby improving its stability under harsh acidic conditions (Figure 5e).[16,23]

Additionally, the original entangled bundle and network structure of HEA NW@NC/SWCNT film remains intact even after prolonged exposure to intense H_2 bubble flush (Figures S29 and S30, Supporting Information), which demonstrates that the membrane electrode is mechanically robust. XPS and XRD characterizations confirm that the composition and phase of HEA NW@NC/SWCNT remain unchanged after 1000 h stability test (Figures S31 and S32, Supporting Information). These results indicate that the well-maintained phase structure and composition of HEA NW@NC/SWCNT can be attributed to the encapsulation effect of the N-doped carbon shells. Compared with previously published results, our HEA NW@NC/SWCNT shows outstanding HER stability at high current densities (Figure 5f; Table S4, Supporting Information). The excellent durability endows the integrated HEA NW@NC/SWCNT membrane electrode great potential as a membrane electrode for large-scale H_2 production.

To evaluate the practical application potential in PEMWE, membrane electrode assemblies (MEAs) were fabricated using HEA NW@NC/SWCNT or commercial 20% Pt/C as the cathode catalysts and commercial IrO_2 as the anode. The performance of these MEAs was systematically assessed (Figure S33a,b, Supporting Information). The IrO_2||HEA NW@NC/SWCNT configuration required a cell voltage of only 1.89 V to achieve a current density of 500 mA cm^{-2}, outperforming the IrO_2||Pt/C (2.42 V) configuration under the same conditions (Figure S34, Supporting Information). Furthermore, the PEM electrolyzer incorporating HEA NW@NC/SWCNT demonstrated remarkable stability, maintaining a consistent current density of 500 mA cm^{-2} with negligible decay over 100 h (Figure S35, Supporting Information). These results indicate that the HEA NW@NC/SWCNT membrane electrode holds significant promise for application in PEMWE devices.

3. Conclusion

A HEA NW@NC/SWCNT integrated membrane electrode composed of N-doped carbon connected to HEA NW and SWCNT network was fabricated. The N-doped carbon shell functions in modulating the electronic structure of HEA NWs and preventing the aggregation, dissolution, and detachment of HEA NWs. The HEA NW@NC/SWCNT integrated membrane electrodes simultaneously showed an ultralow overpotential of 42 mV at 100 mA cm^{-2} and a low Tafel slope of 21.2 mV dec^{-1}. The mass

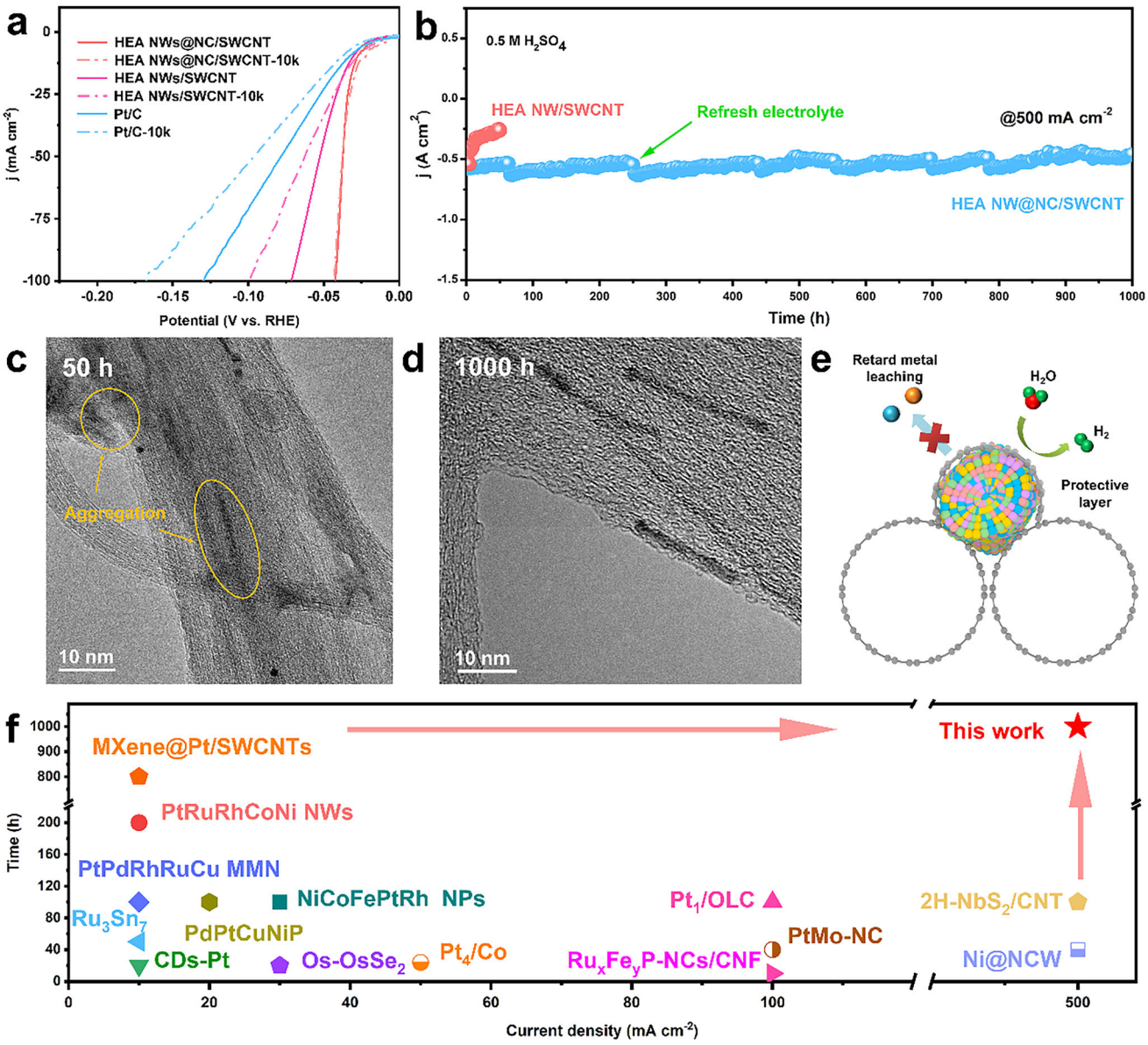

Figure 5. a) HER LSVs before and after 10k cycles. b) Current-time *i–t* chronoamperometric curve at 500 mA cm^{-2}. TEM images of c) HEA NW/SWCNT after 50 h and d) HEA NW@NC/SWCNT after 1000 h. e) Schematic of HEA NW@NC/SWCNT for HER in an acidic solution. f) HER stability of HEA NW@NC/SWCNT compared with that of previously reported representative electrocatalysts.

activity of HEA NW@NC/SWCNT is 18 times higher than that of Pt/C (0.12 A mg^{-1}_{Pt}). Besides, the HEA NW@NC/SWCNT membrane electrode also showed excellent durability, as demonstrated by continuously working for 1000 h at a high current density of 500 mA cm^{-2} in an acidic solution without decay.

4. Experimental Section

Chemicals and Materials: All reagents used are analytical grade purity without purification. Platinum(II) acetylacetonate ($Pt(acac)_2$, 97%), Iron(III) acetylacetonate ($Fe(acac)_3$, 98%), Cobalt(III) acetylacetonate ($Co(acac)_3$, 98%), Nickel(II) acetylacetonate ($Ni(acac)_3$, 95%), Hexadecyl trimethyl ammonium Bromide (CTAB) and Molybdenum hexacarbonyl ($Mo(CO)_6$, 98%) were bought from Macklin. Glucose, ethanol, sulfuric acid (98%), nitric acid (68%), and hydrogen peroxide (30%) were bought from Sinopharm Chemical Reagent Co., Ltd.

Synthesis of SWCNT Films: Raw SWCNTs were synthesized using a floating catalyst chemical vapor deposition (FCCVD) method, as reported in the previous work.[24] After purification and dispersion, SWCNT films were prepared by a filtration method.[14] Due to the high growth temperature (>1000 °C), the SWCNTs prepared by FCCVD have high crystallinity (G/D > 140) and long lengths (>100 µm), enabling them to form free-standing films with good mechanical and electrical properties.

Preparation of HEA NW@NC/SWCNT Films: 40 mg CTAB was added to 5 ml of oleylamine. Subsequently, the mixed solution was ultrasonicated for 30 min. Then $Pt(acac)_2$ (10 mg), $Ni(acac)_2$ (4 mg), $Co(acac)_3$

(8 mg), $Fe(acac)_3$ (8 mg), $Mo(CO)_6$ (10 mg), and glucose (60 mg) were dissolved in oleylamine. Subsequently, SWCNT films were added to the mixed solution and treated by ultrasonication in a constant temperature water bath (60 °C) for 2 h. The mixture was then heated in an oil bath at 220 °C for 1 h. After that, the composite film was taken out and dried in a blast drying oven at 60 °C, and then placed on a graphite plate for fast-heating (JH3.3-P). The temperature reached 700 °C within 30 s, and HEA NW@NC/SWCNT membrane electrodes were obtained. The heating temperatures were tuned as 600, 700, 800, and 900 °C, and the heating times were 25, 30, 35 or 40 s.

Synthesis of HEA NP@NC/SWCNT Films: All parameters are identical with the synthesis of HEA NW@NC/SWCNT, except that the composite film was subsequently heated in a tube furnace. The temperature of the furnace was increased to 700 °C with a heating rate of 10 °C min^{-1}. After that, HEA NP@NC/SWCNT hybrid films were obtained.

Synthesis of HEA NW@NC/Graphene: In the case of the synthesis of HEA NW@NC/graphene, graphene was introduced to replace the SWCNT, while the other conditions were same as the synthesis of HEA NW@NC/SWCNT films.

Synthesis of Pt NW@NC/SWCNT: All parameters are identical with the synthesis of HEA NW@NC/SWCNT, except for that $Pt(acac)_2$ was used in the wet chemical process.

Synthesis of HEA NW/SWCNT: For the synthesis of HEA NW/SWCNT, all conditions are same as the preparation of HEA NW@NC/SWCNT. To remove the organic residuals such as CTAB and oleylamine, the hybrid film was washed three times with a mixture of cyclohexane/ethanol ($V_{cyclohexane}/V_{ethanol}$ = 1:9). After that, HEA NW/SWCNT hybrid films were obtained.

Synthesis of 20 wt.% Pt/C Electrode: Commercial 20 wt.% Pt/C powder (5 mg) was dispersed in a solution of 750 µl ethanol and 250 µl 5 wt.% Nafion, and catalyst ink was obtained. The catalyst ink was ultrasonicated for 20 min. Subsequently, 50 µl of the catalyst ink was drop-cast onto the surface of the SWCNT film. The resulted film was then cut to obtain a free-standing Pt/C electrode with a size of 0.5 × 0.5 cm.

Characterization: Scanning electron microscope (SEM, Verios G4 UC, operating at 10 KV) and transmission electron microscopy (TEM, Tecnai F20, operating at 200 KV) were used to observe the sample morphologies. HADDF-STEM images and EDS mapping were collected using a Titan Cubed Themis G2300 microscope (operating at 300 KV) with spherical aberration. The X-ray diffraction (XRD) patterns were collected using a D8A diffractometer equipped with a graphite-filtered $Cu_{k\alpha}$ source (λ = 0.154 nm), and the scanning range of 2θ is 30–90°. The X-ray photoelectron spectroscopy (XPS) analysis was performed on ESCALAB 250 equipped with an Al Kα excitation source, and the binding energies were rectified by the C1s peak located at 284.6 eV. Inductively Coupled Plasma-Optical Emission Spectrometer (ICP-OES) measurements were conducted using an Advantage Spectrometer (PerkinElmer 8300). Raman analysis is conducted using a micro-Raman system (WITec alpha300 R) with a 532 nm laser. N_2 adsorption-desorption isotherms and pore size distributions were collected on ASAP 2020 M.

Electrochemical Measurements: All electrochemical measurements were performed using a standard three-electrode cell on a CHI 760E electrochemical workstation. The measurements were performed in 0.5 M H_2SO_4 at room temperature. The HEA NW@NC/SWCNT film with an effective area of 0.25 cm^{-2} was used as the working electrode. Ag/AgCl electrode and platinum foil were used as reference electrode and counter electrode, respectively. All potentials were calculated with respect to RHE using the following Equation (1):

$$E\,(RHE) = E\,(Ag/AgCl) + 0.198 + 0.059 \times pH \quad (1)$$

In a general procedure of HER, the electrode was first immersed in an Ar-saturated electrolyte for CV scanning with a scan rate of 100 mV s^{-1}. The electrode was activated and stabilized until a stable CV curve was acquired. LSV curves were collected with a scan rate of 5 mV s^{-1}. The LSV tests were repeated several times until a stable polarization curve was obtained. EIS was measured in a frequency range from 10^6 to 0.1 kHz with a 5 mV amplitude. The cycle durability was measured by a chronoamperometric response at 500 mA cm^{-2} for 500 h. Double layer capacitance (C_{dl}) proportionate to the electrochemical surface area (ECSA) was obtained by CV scanning from 0.15 to 0.25 V versus RHE (scan rates: 20, 40, 60, 80, 100, and 120 mV s^{-1}).

Electrochemical Measurements in PEM Electrolyzer: The PEM water electrolyzer was fabricated with symmetrical electrodes each exhibiting a geometric surface area of 1.0 cm^2 for both oxygen and hydrogen evolution reactions, separated by a Nafion 212 electrolyte membrane. The experimental cathode employed a freestanding HEA NW@NC/SWCNT membrane electrode. For comparative evaluation, conventional electrodes were prepared by depositing commercial catalysts IrO_2 NPs (20 wt.%) and Pt/C (20 wt.%) onto SWCNT films through drop-coating methodology, serving as the anode and cathode respectively, following the same method as the 20 wt.% Pt/C electrode. Catalyst loading control achieved ≈1 mg cm^{-2} for both IrO_2 and Pt.

Electrochemical characterization was conducted in 0.5 M H_2SO_4 electrolyte under ambient atmospheric conditions using a CHI 760E electrochemical workstation. The polarization behavior was systematically assessed through LSV at a controlled scan rate of 10 mV s^{-1}, while operational durability was evaluated via chronoamperometric analysis at a constant current density of 500 mA cm^{-2}.

Computational Method: The structural optimization and energy calculations within the DFT framework are carried out using the Vienna Ab initio Simulation Package (VASP) with vdW correction (D3).[25] To accurately describe exchange-correlation energy, the generalized gradient approximation (GGA) with the Perdew–Burke–Ernzerhof (PBE) functional was adopted throughout all calculations. The cluster and NWs HEA model were constructed using a random arrangement coding method based on the elemental ratio from the ICP-OES experimental results. A vacuum layer of ≈20 Å was considered to avoid the interference from the adjacent periodic images. For all geometrical optimizations, convergence criteria were set with the Hellmann-Feynman force on atoms not exceeding 0.01 eV·$Å^{-1}$ and the energy difference less than 10^{-4} eV per atom.

The Gibbs free energy ΔG for HER on HEA can be defined:

$$\Delta G = E_a + E_{ZPE} - TS \quad (2)$$

where ΔE_a, E_{ZPE}, TS are the adsorption energy of hydrogen, zero-point vibration energy correction, and entropy change during hydrogen adsorption, respectively. ΔE_a can be calculated as follows:

$$\Delta E_a = \left(E_{HEA-H} - E_{HEA} - \frac{1}{2}E_{H_2}\right) \quad (3)$$

Supporting Information

Supporting Information is available from the Wiley Online Library or from the author.

Acknowledgements

H.Y., Z.Z., and Z.W. contributed equally to this work, which was supported by the National Key R&D Program of China (2022YFA1203303), the National Natural Science Foundation of China (Grants 52472054, 52130209, 52072376, and 52372054), the Youth Innovation Promotion Association CAS (2022366).

Conflict of Interest

The authors declare no conflict of interest.

Data Availability Statement

The data that support the findings of this study are available from the corresponding author upon reasonable request.

Keywords

HEA nanowires, hydrogen evolution, integrated membrane electrode, N-doped carbon, single-walled carbon nanotube

Received: December 19, 2024
Revised: February 23, 2025
Published online:

[1] P. Wang, X. Zhang, J. Zhang, S. Wan, S. Guo, G. Lu, J. Yao, X. Huang, *Nat. Commun.* **2017**, *8*, 14580.
[2] S. J. Davis, N. S. Lewis, M. Shaner, S. Aggarwal, D. Arent, I. L. Azevedo, S. M. Benson, T. Bradley, J. Brouwer, Y.-M. Chiang, C. T. M. Clack, A. Cohen, S. Doig, J. Edmonds, P. Fennell, C. B. Field, B. Hannegan, B.-M. Hodge, M. I. Hoffert, E. Ingersoll, P. Jaramillo, K. S. Lackner, K. J. Mach, M. Mastrandrea, J. Ogden, P. F. Peterson, D. L. Sanchez, D. Sperling, J. Stagner, J. E. Trancik, et al., *Science* **2018**, *360*, eaas9793.
[3] a) S. Jiao, X. Fu, S. Wang, Y. Zhao, *Energy Environ. Sci.* **2021**, *14*, 1722; b) N. Du, C. Roy, R. Peach, M. Turnbull, S. Thiele, C. Bock, *Chem. Rev.* **2022**, *122*, 11830.
[4] a) Z. Li, J. Zou, X. Xi, P. Fan, Y. Zhang, Y. Peng, D. Banham, D. Yang, A. Dong, *Adv. Mater.* **2022**, *34*, 2202743; b) M. Li, K. Duanmu, C. Wan, T. Cheng, L. Zhang, S. Dai, W. Chen, Z. Zhao, P. Li, H. Fei, Y. Zhu, R. Yu, J. Luo, K. Zang, Z. Lin, M. Ding, J. Huang, H. Sun, J. Guo, X. Pan, W. A. Goddard, P. Sautet, Y. Huang, X. Duan, *Nat. Catal.* **2019**, *2*, 495.
[5] a) Y. Han, H. Duan, W. Liu, C. Zhou, B. Wang, Q. Jiang, S. Feng, W. Yan, T. Tan, R. Zhang, *Appl. Catal., B* **2023**, *335*, 122898; b) Z. Jiang, W. Zhou, C. Hu, X. Luo, W. Zeng, X. Gong, Y. Yang, T. Yu, W. Lei, C. Yuan, *Adv. Mater.* **2023**, *35*, 2300505; c) J. Kwon, S. Sun, S. Choi, K. Lee, S. Jo, K. Park, Y. K. Kim, H. B. Park, H. Y. Park, J. H. Jang, H. Han, U. Paik, T. Song, *Adv. Mater.* **2023**, *35*, 2300091.
[6] a) G. Feng, F. Ning, J. Song, H. Shang, K. Zhang, Z. Ding, P. Gao, W. Chu, D. Xia, *J. Am. Chem. Soc.* **2021**, *143*, 17117; b) Y. Kang, O. Cretu, J. Kikkawa, K. Kimoto, H. Nara, A. S. Nugraha, H. Kawamoto, M. Eguchi, T. Liao, Z. Sun, T. Asahi, Y. Yamauchi, *Nat. Commun.* **2023**, *14*, 4182; c) W. Shi, H. Liu, Z. Li, C. Li, J. Zhou, Y. Yuan, F. Jiang, K. Fu, Y. Yao, *SusMat* **2022**, *2*, 186.
[7] J. Kibsgaard, I. Chorkendorff, *Nat. Energy* **2019**, *4*, 430.
[8] a) C. Wan, R. Li, J. Wang, D.-G. Cheng, F. Chen, L. Xu, M. Gao, Y. Kang, M. Eguchi, Y. Yamauchi, *Angew. Chem., Int. Ed.* **2024**, *63*, 202404505; b) P. Liu, A. Klyushin, P. Chandramathy Surendran, A. Fedorov, W. Xie, C. Zeng, X. Huang, *ACS Nano* **2023**, *17*, 24395.
[9] a) Y. Liu, J. Ding, F. Li, X. Su, Q. Zhang, G. Guan, F. Hu, J. Zhang, Q. Wang, Y. Jiang, B. Liu, H. B. Yang, *Adv. Mater.* **2023**, *35*, 2207114; b) Y. Li, W. Wang, M. Cheng, Y. Feng, X. Han, Q. Qian, Y. Zhu, G. Zhang, *Adv. Mater.* **2023**, *35*, 2206351.
[10] a) Y. Luo, Z. Zhang, F. Yang, J. Li, Z. Liu, W. Ren, S. Zhang, B. Liu, *Energy Environ. Sci.* **2021**, *14*, 4610; b) M. Zhou, C. Cheng, C. Dong, L. Xiao, Y. Zhao, Z. Liu, X. Zhao, K. Sasaki, H. Cheng, X. Du, J. Yang, *Adv. Energy Mater.* **2023**, *13*, 2202595.
[11] a) R. Cao, R. Thapa, H. Kim, X. Xu, M. Gyu Kim, Q. Li, N. Park, M. Liu, J. Cho, *Nat. Commun.* **2013**, *4*, 2076; b) C. Cui, R. Cheng, H. Zhang, C. Zhang, Y. Ma, C. Shi, B. Fan, H. Wang, X. Wang, *Adv. Funct. Mater.* **2020**, *30*, 2000693; c) R. Gao, Q. Dai, F. Du, D. Yan, L. Dai, *J. Am. Chem. Soc.* **2019**, *141*, 11658.
[12] a) S. Zhu, L. Ding, X. Zhang, K. Wang, X. Wang, F. Yang, G. Han, *Angew. Chem., Int. Ed.* **2023**, *62*, 202309545; b) J. Su, C. B. Musgrave, Y. Song, L. Huang, Y. Liu, G. Li, Y. Xin, P. Xiong, M. M.-J. Li, H. Wu, M. Zhu, H. M. Chen, J. Zhang, H. Shen, B. Z. Tang, M. Robert, W. A. Goddard, R. Ye, *Nat. Catal.* **2023**, *6*, 818.
[13] A. Majeed, P.-X. Hou, F. Zhang, H. Tabassum, X. Li, G.-X. Li, C. Liu, H.-M. Cheng, *Adv. Sci.* **2019**, *6*, 1802177.
[14] Z. Zhang, H. Yang, F. Zhang, M. Zou, J.-C. Li, L. Zhang, P.-X. Hou, C. Shi, L. Zhang, H.-M. Cheng, C. Liu, *Nano Energy* **2024**, *123*, 109356.
[15] a) S. Choudhary, K. Sahu, A. Bisht, B. Satpati, S. Mohapatra, *Appl. Surf. Sci.* **2021**, *541*, 148484; b) B. Ren, M. Cao, Q. Zhang, J. Huang, Z. Zhao, X. Jin, C. Li, Y. Shen, L. Wang, *J. Alloys Compd.* **2016**, *659*, 74.
[16] C. Zhan, Y. Xu, L. Bu, H. Zhu, Y. Feng, T. Yang, Y. Zhang, Z. Yang, B. Huang, Q. Shao, X. Huang, *Nat. Commun.* **2021**, *12*, 6261.
[17] Z. Sun, C. Li, J. Lin, T. Guo, S. Song, Y. Hu, Z. Zhang, W. Yan, Y. Wang, Z. Wei, F. Zhang, K. Zheng, D. Wang, Z. Li, S. Wang, W. Chen, *ACS Nano* **2024**, *18*, 13286.
[18] a) Y. Liu, H. T. D. Bui, A. R. Jadhav, T. Yang, S. Saqlain, Y. Luo, J. Yu, A. Kumar, H. Wang, L. Wang, V. Q. Bui, M. G. Kim, Y. D. Kim, H. Lee, *Adv. Funct. Mater.* **2021**, *31*, 2010718; b) J. Kim, M. K. Kabiraz, W. Lee, G. H. Hwang, S.-I. Choi, *ChemElectroChem* **2020**, *7*, 2643.
[19] L. Tao, Y. Wang, Y. Zou, N. Zhang, Y. Zhang, Y. Wu, Y. Wang, R. Chen, S. Wang, *Adv. Energy Mater.* **2020**, *10*, 1901227.
[20] K. Hu, T. Ohto, L. Chen, J. Han, M. Wakisaka, Y. Nagata, J.-I. Fujita, Y. Ito, *ACS Energy Lett.* **2018**, *3*, 1539.
[21] a) J.-l. Shui, C. Chen, J. C. M. Li, *Adv. Funct. Mater.* **2011**, *21*, 3357; b) W. J. Pech-Rodríguez, D. González-Quijano, G. Vargas-Gutiérrez, C. Morais, T. W. Napporn, F. J. Rodríguez-Varela, *Appl. Catal., B* **2017**, *203*, 654; c) M. Li, Z. Zhao, T. Cheng, A. Fortunelli, C.-Y. Chen, R. Yu, Q. Zhang, L. Gu, B. V. Merinov, Z. Lin, E. Zhu, T. Yu, Q. Jia, J. Guo, L. Zhang, W. A. Goddard, Y. Huang, X. Duan, *Science* **2016**, *354*, 1414.
[22] a) X. Yang, Y. Wang, X. Tong, N. Yang, *Adv. Energy Mater.* **2022**, *12*, 2102261; b) J. Zhao, B. Chen, F. Wang, *Adv. Mater.* **2020**, *32*, 2004142.
[23] a) H. Ma, Z. Chen, Z. Wang, C. V. Singh, Q. Jiang, *Adv. Sci.* **2022**, *9*, 2105313; b) H. Yin, S. Zhao, K. Zhao, A. Muqsit, H. Tang, L. Chang, H. Zhao, Y. Gao, Z. Tang, *Nat. Commun.* **2015**, *6*, 6430.
[24] S. Jiang, P.-X. Hou, M.-L. Chen, B.-W. Wang, D.-M. Sun, D.-M. Tang, Q. Jin, Q.-X. Guo, D.-D. Zhang, J.-H. Du, K.-P. Tai, J. Tan, E. I. Kauppinen, C. Liu, H.-M. Cheng, *Sci. Adv.* **2018**, *4*, eaap9264.
[25] a) G. Kresse, J. Furthmüller, *Phys. Rev. B* **1996**, *54*, 11169; b) G. Kresse, J. Furthmüller, *Comput. Mater. Sci.* **1996**, *6*, 15.